# Chapter 5
# Laser Ablation and Thin Film Deposition

**Christof W. Schneider and Thomas Lippert**

**Abstract** One of the most versatile deposition techniques in solid-state physics and analytical chemistry is the vaporization of condensed matter using photons. A short-pulsed high-power laser beam is focused onto a sample surface thereby converting a finite volume of a solid instantaneously into its vapor phase constituents such as ions and neutrals. Subsequently, the vapor moves away from the target at a high velocity and can be sampled either to grow a film or being analyzed by various spectroscopic techniques. In this chapter, the focus is on general properties of pulsed laser ablation relevant for solid-state physics like the initial ablation processes, plume formation, and plume properties. Next, oxide thin film growth will be discussed and the growth of $LaAlO_3/SrTiO_3$ heterostructures is presented as one example of tailoring oxide interfaces with surprising properties. The final discussion is on the topic of polymer ablation.

## 5.1 Pulsed Laser Ablation

Pulsed laser deposition (PLD) is a growth technique in which the photon energy of a laser characterized by pulse duration and laser frequency interacts with a bulk material [1–3]. As a result, material is removed from the bulk depending on the absorption properties of the target materials. The principle of PLD is shown in Fig. 5.1a. A laser pulse is focused onto the surface of a target (solid or liquid) in a vacuum chamber and thereby removes material. A significant removal of materials occurs above a certain threshold power density, and the ejected, partially ionized material forms a luminous ablation plume. The threshold power density required to create such a plasma depends on the absorption properties of the target material, the laser wavelength, and pulse duration. Typical for excimer laser is a pulse length

C.W. Schneider (✉)
Paul Scherrer Institut, Materials Group, General Energy Research Department,
CH-5232 Villigen PSI, Switzerland
e-mail: christof.schneider@psi.ch

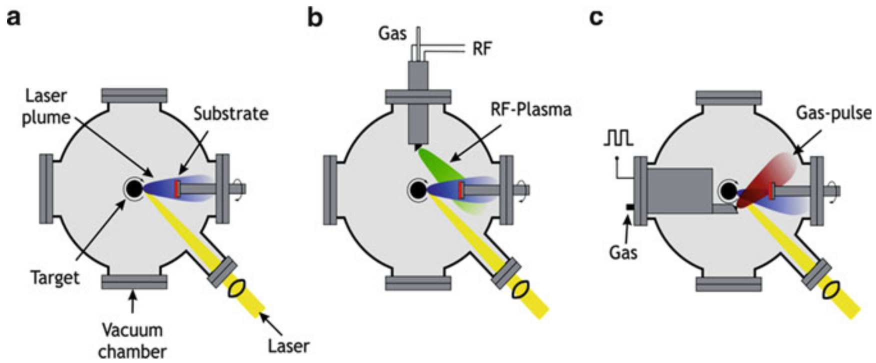


**Fig. 5.1** (**a**) Schematic of pulsed laser deposition (PLD). The incoming laser beam is focused onto a target, thereby vaporizing the material of the surface region. The ejected material is partially ionized and forms the ablation plume which is directed towards the substrate. (**b**) Schematic of a RF-plasma enhanced pulsed laser deposition [4]. (**c**) Schematic of a gas-pulse set-up combined with PLD also known as pulsed reactive crossed beam laser ablation (PRCLA) [5]. The two beams merge after passing the interaction zone and expand together

of 10 ns, for femtosecond excimer lasers it is in the range of 500 fs. The removed material is directed towards a substrate where it recondenses to form a film. The growth kinetic of such films depends on the material flux, repetition rate, growth temperature, substrate material, pressure, and background gas (vacuum, reactive). To enhance the reactivity of the background gas with the ablated species, either a RF-plasma source [4] (Fig. 5.1b) or a gas pulse configuration [5] (Fig. 5.1c) are used.

An interesting development from conventional laser ablation is pulsed reactive crossed beam laser ablation (PRCLA, see Fig. 5.1c). The main feature of PRCLA is the interaction between the ablated plume and a pulsed gas. The purpose of the pulsed gas valve is to use a reactive gas when transfer and deposition of material occurs, but also to provide a higher partial pressure during the interactions, yet to maintain a defined and low background pressure. This can be achieved experimentally by using a distance of at most 1 cm between the nozzle and the ablation point on the target, which results in a strong degree of scattering between the gas and the plume species also called interaction region (see Fig. 5.1c). After passing the interaction region, the initial two beams merge and expand together almost collision-free while maintaining their reactivity for the film growth [6]. One application of the gas pulse is to provide more reactive oxygen by injecting $N_2O$ into the laser plume. As a result, the oxygen content in an oxide film can be improved [7]. Another example is the controlled substitution of ions in a growing film like N-doped $SrTiO_3$ [8, 9]. Here, PRCLA is used to provide reactive nitrogen to the background gas and surprisingly, it worked more efficient compared to N-doped $SrTiO_3$ films grown by RF-plasma assisted PLD.

To use PLD for thin film growth has advantages for a number of reasons:

- The flexibility in wavelength and power density allows to ablate almost any material or materials combination.
- The laser is not part of the vacuum system. Therefore, a considerable degree of freedom in the ablation geometry is possible.
- The use of a pulsed laser beam enables a precise control over the growth rate.
- The congruent transfer of the composition can be achieved for most ablated material or materials combinations.
- Moderation of the kinetic energy of evaporated species to control the growth properties and growth modes of a film.

There are also disadvantages to perform PLD. Some of them are of a technical nature; some are intrinsic to the ablation process and the electromagnetic interaction between photons and matter [2]:

- The large kinetic energy of some plume species causes resputtering and likewise defects in the substrate surface and growing film.
- An inhomogeneous energy distribution in the laser beam profile gives rise to an inhomogeneous energy profile and angular energy distribution in the laser plume.
- Light elements like oxygen or lithium have different expansion velocities and angular distributions in a plume as compared to heavier elements. Therefore, an addition source to supplement these elements to obtain the desired film composition is required, e.g., adequate background gas or an adapted target composition.
- Due to the high laser energies involved, macroscopic and microscopic particles from the target can be ejected which can be detrimental to the desired properties of films and multilayers.

The latter point can partially be overcome by working with very dense polycrystalline or even single crystalline targets, but it also depends on the absorption and mechanical properties of the target material and laser fluence used.

## 5.2 Lasers Used for Laser Ablation

Many types of pulsed lasers have been used for the ablation of solid materials and ruby lasers were among the first to be applied. At present, laser ablation systems are equipped with either Nd:YAG or excimer lasers. Solid-state Nd:YAG systems are employed because they are relatively inexpensive, require little maintenance, there is hardly any divergence of the laser beam, and they can be easily incorporated into small commercial ablation systems. In addition, the beam profile at the base frequency is in most cases close to a Gaussian or a super-Gaussian distribution. Excimer lasers are based on halogen gas-filled laser cavities rather than solid-state crystals. Handling issues demand greater care and laser devices are rather bulky. However, excimer laser have a much bigger power output and typically provide a better defined beam profile.

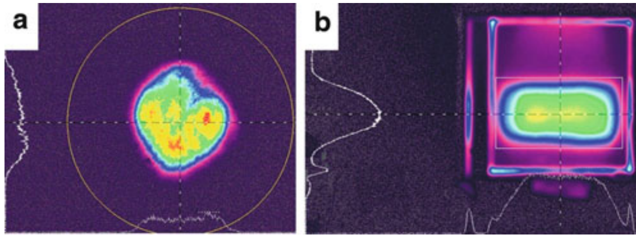


**Fig. 5.2** (**a**) Beam profile of a Nd:YAG operating at $\lambda = 532$ nm. (**b**) Beam profile of a KrF excimer laser operating at $\lambda = 248$ nm. One horizontal and vertical line-scan through the beam profile is shown for each image. Images courtesy of Sven Kern, Spiricon GmbH

To illustrate the differences of the laser beam profile, beam profiles for a Nd:YAG (Quantel Brilliant BW) with $\lambda = 532$ nm and a KrF excimer laser (LPX 100) with $\lambda = 248$ nm are shown in Fig. 5.2. The beam profile for the Nd:YAG at the base frequency of $\lambda = 1{,}064$ nm seems to have not an ideal Gaussian shape which is also observed for the higher harmonics. Several hot-spots are clearly visible in the beam profile in Fig. 5.2a. Contrary to the YAG profile is the flat-top energy distribution for an excimer laser. Such a profile is more homogeneous and hence the energy distribution in a laser plume becomes better defined. The square fringes in Fig. 5.2b are due to the limited size of the image plate used.

The laser wavelength is an important parameter for the ablation process. In general, with decreasing laser wavelength an increase in the ablation rate is expected. For Nd:YAG lasers, the fundamental wavelength is in the near-infrared at 1,064 nm. Optical frequency doubling, tripling, quadrupling, and quintupling (wavelengths at 532, 355, 266, and 213 nm) of the Nd:YAG lasers have been achieved. For excimer lasers, the operating gas determines the lasing wavelength. The excimer laser wavelengths available are at 351, 308, 248, 222, 193, or 157 nm, using XeF, XeCl, KrF, KrCl, ArF, or $F_2$, respectively.

A shorter wavelength offers a higher photon energy which is more suitable for an efficient vaporization and ionization of the solid sample. The equivalent photon energy for a laser wavelength at 266, 213, and 157 nm, is 4.66, 5.83, and 7.90 eV, respectively. However, the absorption properties of a target material will finally decide which laser frequency can be employed. In addition, the chosen wavelength and likewise the pulse length (ns or fs) will affect the laser-induced plasma. In the case of a fs laser-pulse, there is no laser–plasma interaction because the pulse duration is shorter than the time required for a plume to develop.

## 5.3 Initial Ablation Processes and Plume Formation

When a photon interacts with matter, the photon energy is coupled to the lattice through electronic processes. The photon absorption by a material occurs in general over an optical depth of several nanometres where the energy in metals is

transferred to the electronic system directly and in nonmetallic systems typically to the lattice. Electronic relaxation processes are very fast with a typical lifetime of $10^{-14}$–$10^{-13}$ s. For metals it has been shown, that the time scale for the electron energy transfer to the lattice is of the order 1.5 ps and strongly dependent on the thermal conductivity, specific heat, and electron–phonon coupling [6]. For nonmetallic systems, the relaxation time varies between $10^{-12}$ and $10^{-3}$ s. Here, the absorption process occurs on a much shorter time scale compared to the thermal diffusion process, which gives rise to vaporization and plasma formation during the time scale of the pulse duration. The vaporization process can be described by the heat flow theory where the surface temperature of the target at the end of the laser pulse is determined by the light absorption and thermal diffusivity. It is therefore expected that the laser ablation mechanisms for nanosecond and femtosecond ablation are different.

### *5.3.1 Femtosecond Laser Irradiation*

The use of fs pulses in the ablation process, and in particular for nanoparticle synthesis, has been successfully demonstrated [10, 11]. The fs ablation has several advantages compared to longer pulse lengths. First, for a given fluence, higher temperatures and pressures are obtained as compared to ns ablation because the laser energy is delivered before significant thermal conduction occurs. Second, there are no secondary interactions between the laser beam and the ablated material. A higher photon density also means a larger kinetic energy for plume species due to the so-called Coulomb explosion. This is often detrimental for thin film growth as a result of a high-energy ion bombardment of the substrate and growing film. In addition, nanoparticle formation is observed [11–13].

### *5.3.2 Nanosecond Laser Irradiation*

Irradiating a solid with a ns pulse, there is enough time for a thermal wave to propagate into the bulk material thereby causing a melting and evaporation of the material. Two dominant mechanisms are involved in the plume absorption, i.e., inverse Bremsstrahlung and photoionization. These phenomena induce vapor ionization and excitation through collisions with excited and ground state neutrals. ns ablation of metals and ceramics may result at high fluences in the formation of a liquid phase, which is the reason for the ejection of droplets which are embedded in a film. As already pointed out, these drawbacks can be reduced and ns lasers are nowadays a useful tool to grow a large variety of materials.

Having described, how material is ejected from a target upon interaction with the laser photons, the plume formation, and the differences of the ablation process in vacuum and in the presence of a background gas will be discussed next.

When PLD is performed under vacuum conditions, two main aspects are different from sputtering or conventional thermal evaporation techniques. First, pulses of high vapor fluxes ($\sim$1 ms) are separated by periods of no vapor flux ($\sim$100 ms). Second, relatively high vapor arrival energies at the substrate. There may be ions with energies up to the keV range and neutral atoms with energies of several eV.

When PLD is performed in the presence of a background gas like oxygen, two effects are expected during the film formation: (a) the reduction of the kinetic energy of the vapor flux; (b) it provides a high flux of background oxygen molecules bombarding the surface during deposition. This high flux could change the film and substrate surface energies and will increase the oxygen content, like in oxide thin films. Changing the background gas to other gases such as $NH_3$ to provide reactive nitrogen, the composition of a film can be substantially changed [8,9]. Likewise, the introduction of $CH_4$ as background gas to form Si–C or C–N has been successfully demonstrated [14].

## 5.4 Plume Expansion

### *5.4.1 Plume Expansion in Vacuum*

The plume expansion in vacuum is considered adiabatic, as long as there is no mass and energy transfer to the ablation plume and hence the plume expansion is called almost collision free. According to the Anisimov model [15], the plume expansion is characterized by an ellipsoid. As the ablation rate (in ns ablation) exceeds 0.1 monolayer per second, high particle densities are formed at the target surface. Multiple scattering between plume species tends to thermally equilibrate the plasma, resulting in the formation of the so-called Knudsen layer [2]. This Knudsen layer modifies the Maxwell–Boltzmann distribution to a shifted function, which includes the centre of mass velocity given by (5.1):

$$f(v) = A\left(\frac{m}{2\pi k}\right)^{\frac{3}{2}} v^n \exp\left(\frac{-m(v-u)^2}{2kT}\right) \mathrm{d}v, \tag{5.1}$$

where $m$ is the mass of the particles, $k$ is the Boltzmann constant, $v$ is the speed along the propagation direction, $u$ is the stream velocity, $T$ is the stream speed, which describes the angular distribution of the propagation, and $n$ is an integer (typically 3–4).

### *5.4.2 Plume Expansion into a Background Gas*

A background gas can be utilized to reduce the kinetic energy of the plume species and to increase the number of chemical reactions between the plume and gas

molecules thereby forming atomic (N, O) and diatomic species. The plume dynamics is affected by the gas type and gas pressure. At a low background pressure (<1 Pa), the plume expansion is similar to the ablation in vacuum. At intermediate background pressures (10–100 Pa), the background gas influences progressively the plume dynamics. During the plume expansion in a background gas, it pushes gas away thereby introducing a compression of the gas and of the plasma plume. If the mean free path of the plume species is reduced, a shock wave is formed and the plume pressure equalizes the background pressure [16]. According to the model of Zeldovich and Raizer, the plume mass can be determined as follows:

$$M_p \approx \frac{2}{3}\pi R_{\mathrm{SKW}}^3 \rho_{\mathrm{g}}, \tag{5.2}$$

where $\rho_{\mathrm{g}}$ represents the gas density and $R_{\mathrm{SKW}}$ is the distance at which the hemispherical shock wave starts.

The spherical expansion, calculated using the blast wave model can be described as

$$R_{\mathrm{b.w.}}(t) = \varepsilon_0 \left(\frac{2E_0}{\rho_{\mathrm{g}}}\right)^{\frac{1}{5}} t^{\frac{2}{5}}, \tag{5.3}$$

where $\varepsilon$ and $\rho$ are constants determined by the specific heat ratio and the mass density of the layer.

At pressures larger than 100 Pa, a strong confinement of the plume with a short stopping distance takes place. For the laser ablation of $LaMnO_3$, a stopping distance smaller than 1 cm was reported [10].

### 5.4.3 *Imaging*

Having discussed in the previous sections the properties of the laser plume expansion, we discuss next the laser plume expansion in vacuum and in a background gas. The laser plume expansion by imaging the emission of neutral Mn-plume species (Mn I) in vacuum and at a background pressure of 20 Pa oxygen at different times after the laser pulse strikes the target are shown in Fig. 5.3 [17]. Here, a laser with $\lambda = 248$ nm was focused on a rotating $LiMn_2O_4$ target at an incident angle of 45° with a laser fluence 2 $\mathrm{Jcm^{-2}}$ and a spot size on the target of 1 $\mathrm{mm^2}$. Emission spectra measurements were performed in a high vacuum chamber at a base pressure of $\sim 10^4$ Pa and recorded with an intensified charged couple device (ICCD, DH520-18F, Andor technology) gated for an interval of 40 ns.

The emission images for Mn I in vacuum are shown in (Fig. 5.3a), with the delay time indicated in each frame. A hemispherical expansion of the Mn I plume is observed for all time frames except at longer times when the plume becomes more elongated. For the ionized Mn species (Mn II), the plume expansion is comparable in time with Mn I. For Li I however, the initial hemispherical expansion becomes elongated which is attributed to the high velocity of the expanding species (see

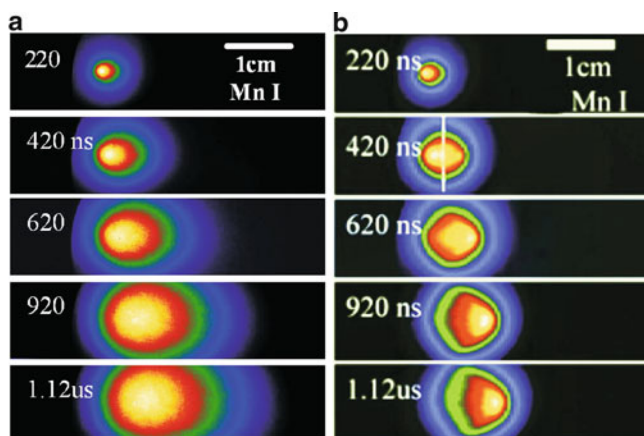


**Fig. 5.3** ICCD emission images of neutral Mn-plume species as obtained by ablating $LiMn_2O_4$ in (**a**) vacuum and (**b**) at 20 Pa of oxygen. Each image is normalized with respect to the maximum intensity. The laser fluence for the KrF-laser was set to 2 $Jcm^{-2}$ with a laser spot on the target of 1 $mm^2$ [17]

**Table 5.1** Excited state lifetime and the expansion velocities in vacuum and in an oxygen background for neutral Mn and Li-species are given [17]

| Species | Excited state lifetime (nsec) | Expansion velocity in vacuum (m/s) | Expansion velocity in 20 Pa $O_2$ (m/s) |
|---|---|---|---|
| Mn I | 5 | 1.2 ($\pm$0.01)$\times 10^4$ | 7.8 ($\pm$0.01)$\times 10^3$ |
| Li I | 27 | 1.8 ($\pm$0.01)$\times 10^4$ | 1.6 ($\pm$0.01)$\times 10^4$ |

Table 5.1). The plume images for Li I also indicate an increased angular broadening of the plume compared to Mn I.

The plume emission evolution at 20 Pa oxygen background pressure (Fig. 5.3b) for Mn I is very different compared to a vacuum expansion. Here, the plume undergoes multiple scattering with the gas species which results in a sharpening of the plume front. The plume is progressively decelerated, which is revealed by the increase in the emission intensity at the plume front. In addition, interaction of the plasma plume with the background gas leads to a separation of the plume into two main components (Fig. 5.3b, 420 ns). The peak appearing at the plume front gains intensity in time with respect to the peak close to the target surface, while at later times, the two peaks merge. In addition, the velocity of the species slow down and become comparable at the later observation time. The data in Fig. 5.3b also indicate that the emission intensity profiles of Mn I in the background gas are sharper as compared to the emission profiles in vacuum. This is attributed to the confinement of the plume, induced by the collisions of the species in the plume with the background gas.

In Table 5.1, the lifetime of the exited states for Li I and Mn I is given. The lifetime for Li I is ~5 times longer than for Mn I; however, the time over which the plume excitation can be observed is much longer. In optical emission

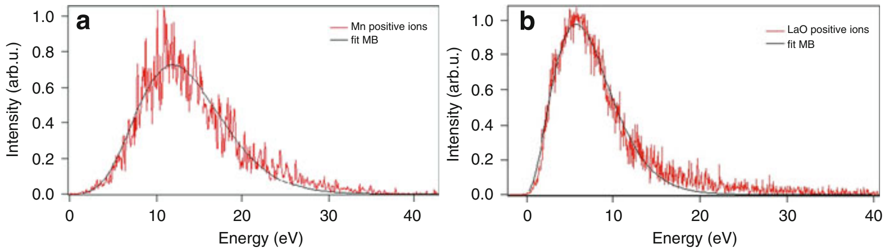


**Fig. 5.4** Kinetic energy distributions of (**a**) $Mn^+$ and (**b**) $LaO^+$ species are measured during the ablation of $La_{1-x}Ca_xMnO_3$ in vacuum with a laser fluence of 1 J/cm$^2$ and a laser wave length of $\lambda$ =193 nm. The fit to the experimental data is based on a shifted Maxwell–Bolzmann (MB) distribution [21]. Images courtesy of Stela Canulescu

spectroscopy, not only excited species created during the ablation process are detected, but also species formed and excited during plume expansion. The observation of plume species over a few hundred ns indicates that excitation processes occurs during the plume expansion. A likely mechanism for an extended observation time is the recombination and reexcitations of plume species due to collisions with electrons and other plume species. This allows for a prolonged detection as shown in Fig. 5.3.

### 5.4.4 *Kinetic Energy of Plume Species*

The kinetic energy and angular distribution of ablated species are the main parameters which determine the plume characteristics and to a large extent the growth mode of a film. In vacuum, the kinetic energy of plume species was found to vary between a few eV and up to ∼80 eV [18]. In the case of the double and triple charged C-species, generated from a graphite target, the mean value of the energy distributions was found to be around 160 and 240 eV, respectively [19]. Also, kinetic energies of up to 100 eV were reported for the ablation of Si, Ge, and Cu. Here, the kinetic energy was found to vary almost linear with the ion charge.

The kinetic energy of laser plume species can be measured using an electrostatic energy analyzer coupled with a quadrupole mass spectrometer (EEA–QMS). The plume species of interest are detected by their energy per charge ratio ($\varepsilon/q$) and subsequently selected in the QMS due to the charge to mass ratio ($q/m$). Hence, this method provides a direct measurement of the kinetic energy distribution for a given mass. An example for a measurement of the kinetic energy of different plume species is given in Fig. 5.4. The kinetic energy distribution was measured for two different positive ions ($Mn^+$ and $LaO^+$) while ablating $La_{1-x}Ca_xMnO_3$ in vacuum with a ArF-Laser and a laser fluence of 1 J/cm$^2$ [20].

Fitting the Maxwell–Bolzmann distribution to the experimental data in Fig. 5.4 allows to extract an effective temperature of the species along the expansion

direction, the centre of mass velocity as well as the so-called most probable energy $E_p$, which corresponds to the maximum peak position of the energy distribution. In vacuum, the ionic species exhibit a centre of mass velocity between $2.5 \times 10^3$ and $1 \times 10^4$ m/s while the velocity of the neutral species varies between $2.4 \times 10^3$ and $4.4 \times 10^3$ m/s. It is interesting to note that in this experiment the oxygen species are among the fastest species in the plume. The most probable kinetic energy for the different species varies between 5 and 10 eV with tails extending well beyond 30 eV. Values obtained for the effective temperature for ionic species are in the range of $1-1.2 \times 10^4$ K ($\sim$1 eV) and for neutral species of the order $2-3 \times 10^3$ K ($\sim$0.3 eV). These extracted numbers underline the fact that the chemistry in such a plasma is far from the chemical equilibrium. To achieve under the described deposition conditions, the correct chemical composition in a film can be difficult due to very different expansion velocities and angular distributions for different species. It is also interesting to point out that the mean kinetic energy for species is comparable or smaller than typical values obtained for sputtering (several 10 eV and larger) but larger than for molecular beam epitaxy ($\sim$0.1 eV). However, the tail end of the kinetic energy distribution can be high and result in detrimental effects on the growth of a film and the corresponding properties. Consequences of the latter point will be illustrated in the section on tailoring interfaces in oxides.

### *5.4.5 Thin Film Growth*

Growing oxide thin films involves a number of requirements. Often, epitaxial growth of a material is preferred and therefore the choice of the appropriate substrate material is important. Basic requirements are a good crystallographic lattice match between film and substrate, the substrate material should be chemically compatible to the film, it should have comparable thermal expansion coefficients, and a thermodynamically and chemically stable surface. Essential for some applications is to choose selectively the chemical termination of the surface [22, 23]. Examples are $SrTiO_3$ substrates with a $TiO_2$-termination (B-site termination) [22] or $NdGaO_3$ with a NdO-termination (A-site termination) [24]. Such surfaces allow the growth of a material from a chemically well-defined surface which minimizes, e.g., line defects in $YBa_2Cu_3O_{7-\delta}$ typically occurring in these films when grown on a surface with a mixed termination [25]. In Fig. 5.5, the growth of (001) oriented $SrRuO_3$ on $TiO_2$-terminated (001) $SrTiO_3$ is depicted. On the left side, the atomic structure of $TiO_2$-terminated (001) $SrTiO_3$ is shown. When growing $SrRuO_3$, the growth will start with a SrO layer compatible to the cubic $SrTiO_3$ lattice followed by a layer of $RuO_2$ rotated by 45° to the initial SrO layer. Only thereafter, the atomic arrangement of $SrRuO_3$ is as expected for the orthorhombic $SrRuO_3$ unit cell.

When species of the plume arrive at a substrate surface, the first arriving pulse causes the nucleation of a high density of smaller clusters. These subcritical clusters tend to dissociate into mobile species that will nucleate new clusters of a different size during the time of no vapor arrival. The next pulse will initiate the same process

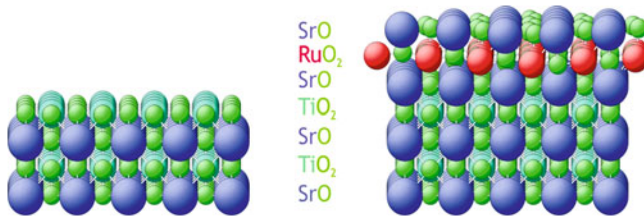


**Fig. 5.5** Atomic model of $TiO_2$-terminated (001) oriented $SrTiO_3$ (*left*). On the right hand side, the initial growth of (001) $SrRuO_3$ on (001) $SrTiO_3$ is depicted. Images courtesy of Izabela Czekaj

again, with the difference that some of the mobile atoms will reach the previous formed clusters. What is the influence of laser wavelength, power density, repetition rate, substrate temperature, and background pressure on the growth properties of a film?

As already discussed, wavelength and power density will determine if the evaporation of the target material will be a thermal or a nonthermal evaporation process. It also determines the ratio between neutral and ionized species in a plume. The repetition rate will determine the degree of supersaturation of the evaporated material on the surface of the substrate which has a direct influence on the growth mode of a growing film. The substrate temperature is important to ensure a sufficient surface mobility of the arriving species to support epitaxial growth. To obtain the correct film composition, the background pressure and gas is another parameter which needs to be controlled. For most oxides, an oxygen atmosphere is necessary for the correct oxygen content in a film, some materials require a reducing atmosphere, like for $LaTiO_{3-x}$ [26, 27]. The chemistry of a film can also be controlled by the background gas as discussed for the growth of oxynitrates [8, 9]. Another example is the growth of NbN in a nitrogen atmosphere using PLD [28] or growing NbN/MgO heterostructures [29], where the background gas has to be changed for each material.

What are the different growth modes for epitaxial films [30, 31]? Ideally, the free energy of the substrate surface which depends on the crystalline orientation of the surface, the free energy of the film surface and the free energy of the interface need to be minimized. The latter point includes the misfit between substrate and film. This leads either to the ideal 2D layer-by-layer growth of a film (Fig. 5.6a), an island growth mode (Fig. 5.6b), or a layer-by-layer growth followed by an island growth mode (Fig. 5.6c). An island growth occurs when atoms or molecules in a growing film are more strongly bound to each other than to the substrate thereby forming clusters. A layer-by-layer growth requires species with a high mobility on a surface provided by the kinetic energy of the arriving species and the surface temperature of the substrate. In addition, a good lattice match is necessary. The surface roughness is the result of the incomplete coverage during the growth of one monolayer. A 2D growth followed by an island growth is often the result of a strain release of a growing film due to the lattice mismatch between substrate and film.

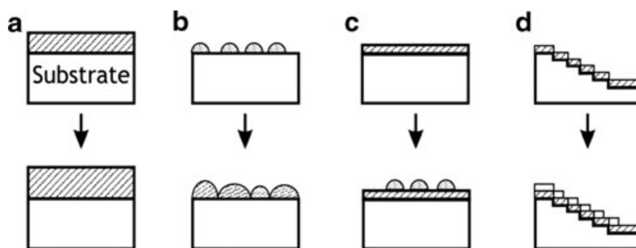


**Fig. 5.6** Schematic illustrating four different growth modes for epitaxial growth: (**a**) 2D layer-by-layer growth (Frank–van der Merwe), (**b**) 3D island growth (Volmer-Weber), (**c**) layer-by-layer followed by an island growth (Stranski–Krastanov), and (**d**) step-flow growth

The surface of a crystal or the crystal itself is often not ideal. Defects are present which promote, e.g., the growth of screw dislocation in a film as a mechanism to accommodate the defect structure of the seed crystal. One example is the formation of screw dislocations in $YBa_2Cu_3O_{7-\delta}$ grown on $SrTiO_3$ [32]. The surface is never ideally flat, but has a certain miscut and hence the surface consists of terraces with a finite width. If the distance mobile species can move on a surface is larger than the terrace width, step-flow growth occurs (Fig. 5.6d). This type of growth mode depends on the growth temperature, substrate miscut, and the supersaturation of the arriving species. The degree of supersaturation can also switch between screw dislocation mediated growth and step-flow growth [33].

Another type of relaxation mechanism is the strain release via misfit-dislocations. If a heteroepitaxially grown film is thinner than a critical thickness $t_c$, it grows coherent and highly strained (tensile or compressive strain). For films with $t > t_c$, the strain is released by a build-in misfit-layer. In case the tension cannot be relaxed by a misfit layer, such a film will develop cracks when reaching $t_c$. An example for crack formation in a highly strained film is shown in Fig. 5.7b. Here, 102 uc of $LaAlO_3$ have been grown epitaxially on $TiO_2$-terminated (001) oriented $SrTiO_3$. In Fig. 5.7a, 5 uc of $LaAlO_3$ have been grown epitaxially on $SrTiO_3$ in a 2D growth mode, monitored using high pressure RHEED (reflective high-energy electron diffraction) [34]. The 2D growth, expressed here as the step and terrace growth of $LaAlO_3$ can be maintained even to a layer thickness of 102 uc. At a threshold thickness $t_c$ of 25 uc, crack formation starts and becomes very pronounced with increasing $t$ with the underlying substrate terraces still clearly to be observed (Fig. 5.7b). In Fig. 5.7c, the STEM cross-sectional image of such a layered structure shows a highly coherent and strained layer of $LaAlO_3$ on $SrTiO_3$ with the unit cell lattice parameter of $LaAlO_3$ (a(LAO) = 0.3,791 nm) equals that of $SrTiO_3$ (a(STO) = 0.3,906 nm). Despite the high biaxial tensile strain of $\approx$3%, $LaAlO_3$ grows over tens of nm without a visible defect even for thicker layers of $LaAlO_3$.

Another type of defect, inherent to the epitaxial growth of oxide thin films is twinning. Growing a material with an orthorhombic structure like $YBa_2Cu_3O_{7-\delta}$ on a cubic seed lattice ($SrTiO_3$), there will be no preferential orientation for the in-plane lattice parameters of the orthorhombic film. Hence, such a film will be twinned. To

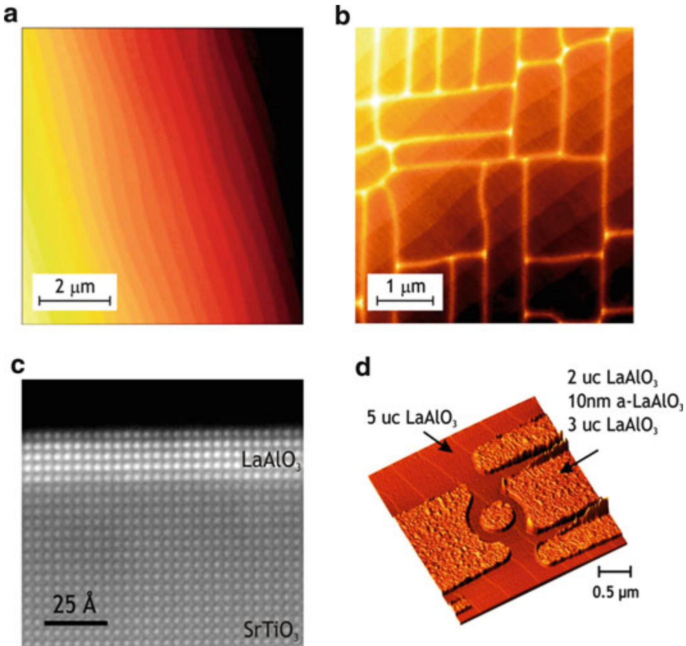


**Fig. 5.7** (**a**) Topographic AFM-image of a 5 uc $LaAlO_3$ thick layer on a $TiO_2$ terminated $SrTiO_3$ substrate. The uc high terraced structured of the substrate is preserved in the $LaAlO_3$ layer. (**b**) Topographic image of a 102 uc $LaAlO_3$ thick layer on a $TiO_2$-terminated $SrTiO_3$ substrate. Like in (**a**), the terraced structure of the substrate is preserved. In addition, a very pronounced crack formation in the $LaAlO_3$-layer has taken place. The critical thickness for cracks to appear is 25 uc. (**c**) Cross-sectional high angle annular dark field (HAADF) STEM image of a 5 uc thick layer of $LaAlO_3$ (*bright*) on a (001) oriented $SrTiO_3$ substrate (*greyish*). The contrast between $LaAlO_3$ and $SrTiO_3$ is dominated by a chemical contrast. (**d**) AFM image of a ring as defined by the sequential deposition of epitaxial and amorphous $LaAlO_3$. The epitaxially grown area defines a 2D electron gas inside the ring with a diameter of $\approx 1.2\,\mu m$ and a track width of of $\approx 200$ nm [35]. AFM images courtesy of S. Thiel, G. Hammerl, and J. Mannhart, University of Augsburg (Germany). STEM image courtesy of L. Fitting Kourkoutis and D.A. Muller, University of Cornell (USA)

achieve in the ideal case a twin-free growth, the substrate lattice constant can be matched to the lattice of the orthorhombic film with a defined miscut of the substrate in one crystallographic direction. This idea of a defined substrate matching has been successfully demonstrated for the growth of $YBa_2Cu_3O_{7-\delta}$ thin films on $SrTiO_3$ with a substrates miscut of $\approx 1°$ either along the (100) or (010) direction. The grown $YBa_2Cu_3O_{7-\delta}$ films are almost twin-free with single crystalline normal state and superconducting transport properties [36, 37].

*Film growth and properties of $LaAlO_3$/$SrTiO_3$ interfaces*

An outstanding example of surface engineering and the influence of the proper interface termination has been discovered in the $LaAlO_3$/$SrTiO_3$, $LaTiO_3$/$SrTiO_3$, and $LaVaO_3$/$SrTiO_3$ system [38–40], where a metallic-like interface conductivity is confined to a few unit-cells at the interface [41]. One way to explain the

observed conductivity is by oxygen defects which cause conductivity in $SrTiO_3$ [42–44]. Considering the stacking sequence of $LaAlO_3$ on $SrTiO_3$, there is an alternative explanation of this interface conductivity which is based on the polarity discontinuity at the interface between the $TiO_2$-terminated $SrTiO_3$ and the homoepitaxially grown $LaAlO_3$ [45]. Looking at the $SrTiO_3$ sub-unit cells, the charge neutral $SrO^0$ is followed by $TiO_2^0$, whereas for $LaAlO_3$, positively charged $LaO^+$ is followed by negatively charged $AlO_2^-$. At such an interface (Fig. 5.8a), a Coulomb potential of several eV can build up. One way to lower the potential barrier is to move charge from the top surface to the interface corresponding to an electronic reconstruction at the interface (Fig. 5.8b). Another way to explain the conductivity is that defects holding a charge like oxygen vacancies can be moved to the interface by force due to the strong electrostatic potential. This is also known as ionic compensation.

All three mechanisms to explain the interface conductivity have observable consequences based on how these stacking sequences are grown. This will be discussed in the following paragraphs. Typical deposition parameters for $LaAlO_3$ are a deposition temperature ≈750–770°C, a laser fluence of ≈1 $J/cm^2$ and an oxygen background pressure of $2\times10^{-5}$ mbar [34, 38, 39, 46]. The growth mode for $LaAlO_3$ is 2D (Fig. 5.7a). With these parameters, a quasi-2 dimensional conductivity associated with the interface is observed with a charger carrier density of $\approx 3\times10^{13}/cm^2$ between room temperature and 4.2 K and a metallic like temperature dependence for the resistivity [34, 38, 39, 46]. These interfaces even become superconducting when cooled below 200 mK [41, 47]. In the superconducting state, an estimate for the conducting sheet layer thickness reveals an upper limit of 4 nm verifying the 2-dimensional character of the conducting layer [41, 47].

With increasing background pressure up to $\approx 10^{-2}$ mbar, the film surface becomes rougher and the resistivity larger as compared to interfaces grown in the $10^{-5}$ mbar range. The increase in roughness and in resistivity indicates the presence

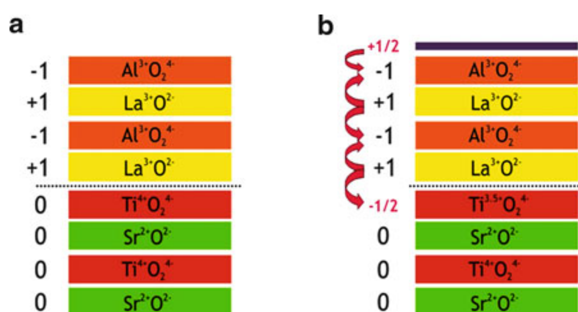


**Fig. 5.8** Illustration of an atomically sharp interface between (001) $LaAlO_3$ and (001) $SrTiO_3$. (**a**) Stacking sequence of an unreconstructed n-type interface between neutral SrO and $TiO_2$ planes followed by charged $LaO^+$ and $AlO_2^-$ planes. This stacking sequence causes a diverging potential at the interface with an increasing number of $LaO^+$ and $AlO_2^-$ planes. (**b**) The diverging potential can be avoided by the transfer of ½ an electron per unit cell from the top surface to the top $TiO_2$ layer [48]

of defects in the $LaAlO_3$ layer due to a change in supersaturation and surface mobility of the arriving species during the deposition. However, at present there are different pressure regimes reported at which significant changes to the electrical and surface properties take place [46, 49]. The role of defects on the transport properties for the 2D-conducting layer has been studied [50]. It is reported that a dislocation in a $SrTiO_3/LaAlO_3$ heterostructure is a scattering center with an insulating and charge-depleted cross section of $\approx$5 nm. One consequence of the presence of defects on the conducting properties of the interface is a significant change in the temperature dependence of the resistance at low temperatures [50]. Similar changes to transport properties in addition with magnetic field-dependent measurements of the resistance are associated with ferromagnetic properties of this interface [46].

Ablating $LaAlO_3$ in a pressure regime well below $10^{-5}$mbar, the kinetic energy of the arriving species becomes more important. As already discussed, the tail end of such an energy distribution can easily reach several tens of eV. Such a medium to higher energy ion-bombardment of $SrTiO_3$ is detrimental to the surface properties. First, a sputtering of the surface creates a finite roughness; second, the ion-damage leads to charged vacancies and hence to a well conducting surface. In addition, the combination of a very low pressure and high temperature is responsible of some oxygen loss and hence oxygen defects near the $SrTiO_3$ surface. Extended defect structures for interfaces prepared at such low pressure have been reported in [43]. The charge carrier density of these heterostructures is of the order $10^{16}/cm^2$ and comparable to numbers measured for oxygen reduced $SrTiO_3$. If such structures are annealed sufficiently long in oxygen, the conductivity originally measured disappears. Subjecting the heterostructures with 2D-conducting interface layers to an extended oxygen heat treatment, the resistance can be changed but the charge carrier density remains effectively unchanged.

There is also the question if the interface is atomically sharp, or is there some intermixing of La and Ti. The STEM image in Fig. 5.7c suggests that the interface is atomically sharp. It is a high angle annular dark field (HAADF) STEM image, where the contrast between the 5 uc $LaAlO_3$ and $SrTiO_3$ is largely due to the chemical difference between La (light) and Sr (dark). If there is some intermixing of La and Sr, it is limited to at most 1 uc. The atomic reconstruction of the $LaAlO_3/SrTiO_3$ interface based on x-ray surface diffraction studies suggests a finite intermixing over at least 1 uc [51]. Further studies to clarify this issue are necessary.

The $SrTiO_3/LaAlO_3$ stacking sequence for the interface as illustrated in Fig. 5.8a has an interesting consequence. The appearance of an interface potential due to the polar nature of the interface will drive an electronic reconstruction only if the build-in potential becomes large enough. Therefore, it can be expected that there will be a threshold thickness for $LaAO_3$ at which a diverging potential due to the increasing number of $LaAlO_3$ layers will drive an electronic reconstruction. In order to bring the potential back to zero, the nominal charge of e/2 has to be transferred from the top-most $AlO_2^-$ layer to the interface as illustrated in Fig. 5.8b [45, 48]. In case, the diverging potential cannot be brought back to zero via a charge transfer to the interface, the structure remains insulating. The existence of such a critical

$LaAlO_3$ layer thickness was verified by Thiel et al. [34] and also confirmed for $LaVaO_3/SrTiO_3$ interfaces [40].

So far, there is no hard experimental indication that an ionic compensation mechanism is the driving force to generate interface conductivity. One way to invoke such a scenario is by applying an external electric field to the $LaAlO_3/SrTiO_3$ heterostructure with the $LaAlO_3$ layer thickness smaller than the critical thickness. There, a threshold voltage is required to obtain the conducting interface [34, 52]. Once, the conducting state is reached and the gate voltage removed, the conducting state is stable in time over several minutes to hours. This is particularly striking for electric field induced AFM written nanostructures, which are stable up to one day at room temperature [52, 53].

Most electrical measurements on this interface have been done on large area samples. For electrical transport measurements, however, a lithographically defined structure would be useful. Ion beam etching of the heterostructure is not practical due to the defect-induced conductivity at the $SrTiO_3$ surface. A useful and simple route to pattern the interface without exposing it to chemicals needed for patterning is provided by the critical layer thickness [35]. The delicate interface is protected prior patterning by two monolayers of epitaxially grown $LaAlO_3$. After the definition of the measurement structure, a second epitaxial layer of $LaAlO_3$ is grown on top of the protecting $LaAlO_3$ layer to obtain the conducting interface wherever it is required. One example of such a pattern is shown in Fig. 5.7d. It is interesting to note, that $LaAlO_3$ can be grown homoepitaxially and in sufficient quality on top of each other despite the extensive use of chemicals on the first $LaAlO_3$ surface.

## 5.5 Laser Ablation of Polymers

Polymers are a class of materials which require low threshold fluences for a gentle processing (reduced energy and heat transfer). This makes them suitable candidates for low power laser ablation. First studies on the laser ablation of polymers were reported in 1982 by Srinivasan [54] and by Kawamura [55] on polyethylene terephtalate and polymethyl methacrylate, respectively. Since, the ablation of polymers developed a variety of applications, ranging from drilling [56] to ophthalmology [57]. For ablation, the UV region of the spectrum is of interest, because it allows involving photochemical degradation which is intrinsically more precise than thermal decomposition. The short wavelength is also advantageous for a precision processing operating at the diffraction limit.

Most commercial polymers absorb below $\lambda = 250$ nm and these polymers can be ablated with the corresponding excimer or Nd:YAG lasers. However, by applying shorter wave length chemical bonds like C-bonds can be broken leading to a carbonization of the surface of these polymers. Therefore, it is advantageous to work in the UV range above $\lambda = 250$ nm. In this frequency range, triazene and pentazadiene chromophores have a high absorption around 300 nm and a XeCl excimer laser ($\lambda = 308$ nm) can be used for ablation. Incorporating triazene and pentazadiene

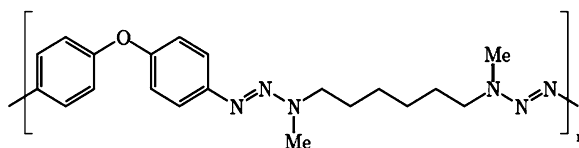


**Fig. 5.9** Chemical structure of the triazene polymer

into the polymer main chain, this yields several related compounds [58]. The most promising candidate for laser ablation, an aryltriazene polymer, is shown in Fig. 5.9. This holds also true if compared to selected commercial or polymers designed for laser ablation, such as polyimides, polyesters [59, 60], or polyurethanes [61, 62].

The aryltriazene polymers show very high ablation rates per pulse, the lowest threshold fluence compared to other polymers and debris-free ablation. These properties make them a promising candidate for an application as a dynamic release layer (DRL) for laser-induced forward transfer (see below).

### *5.5.1 Ablation Mechanism*

While the ablation of polymers is well established, several fundamental aspects of the ablation process are still debated. The difficulty to model the laser ablation of polymers is related to their complex nature (large molecules, possible reactive pathways, etc.) when compared to metals or oxides. Several models have been proposed, which are reviewed in [63, 64] but up to now, these models are only able to describe well the experimental observations for a single class of polymers, i.e., Kapton™.

There are a range of different models to explain the ablation process. They can be divided into photochemical models [65–70], photothermal models [71–74], and photophysical models [75]. There is an effort to combine the presented models because they only partially predict aspects of the ablation of polymers. Some attempts have been made to describe the ablation process by combining the features of the different models mentioned above, thereby creating mixed model [76]. However, this appears to be a very difficult task because the details of the ablation process will always depend on the laser parameters like wavelength, fluence, pulse duration, and the chemical structure of the polymer in question.

What are the applications for polymer ablation? There are at present four directions which can be identified: (a) material removal, (b) deposition, (c) analysis, and (d) miscellaneous. (a) Material removal involves everything related to surface and volume modification with a high lateral and depth resolution. This includes direct patterning of structures thereby combining the definition and etching of a structure in a single step. (b) The deposition of a material on a substrate can either take place as a single continuous film or involves the direct transfer of a pattern. The latter point, also called laser induced transfer, will be discussed separately. (c) The removal of material from a sample can be used for analytical purposes. The ablated plume is imaged and analyzed optically using emission

spectroscopy. The constituents of a plume can also be measured using mass spectrometry, inductively coupled plasma mass spectrometry [77–79], or matrix-assisted laser desorption/ionization–time of flight analysis. All techniques allow the investigation of the initial composition of the target. (d) The fourth direction for applications include plasma thruster for microsatellites, shock wave generation and others niche applications.

### *5.5.2 Polymer Film Ablation*

Like for metals and oxides the direct ablation of polymers in vacuum to deposit polymer films has been achieved [48, 80–82] (Fig. 5.10a). Due to the nature of the ablation process, this works only for certain polymers such as Teflon [81] and PMMA [40, 83, 84]. These polymers depolymerize upon irradiation and subsequently polymerize with a different, most probably lower molecular weight on the substrate. Alternatively, it is proposed that after the depolymerization intact chains are transferred directly onto a substrate [40, 83, 84].

The direct application of a pulsed laser beam is critical when used on sensitive compounds due to the direct irradiation of the material and the absorption of the laser energy. To prevent this, a technique was developed, called matrix-assisted pulsed laser evaporation (MAPLE). The method, shown in Fig. 5.10b, uses a frozen solvent (the matrix) target containing the material to be deposited. Upon irradiation, the solvent is evaporated and forms a plume together with the molecules of interest. Films grown on a substrate consist of dried molecules previously solvated in the matrix [82, 85–87], although recent data have shown that solvent molecules are also trapped in these films [85]. The method is mainly applied to biological molecules (e.g., proteins) or sensitive organic molecules. To avoid or reduce the aforementioned depolymerization, a possibly more gentle transfer of conductive polymers such as MEH-PPV [88, 89] and PEDOT:PSS [90] has been proposed when using a free-electron laser in the mid-infrared domain at the resonant frequency of the solvent.

Although PLD and MAPLE are very useful techniques to prepare thin organic films, they do not conserve the spatial information from the laser impact spot and

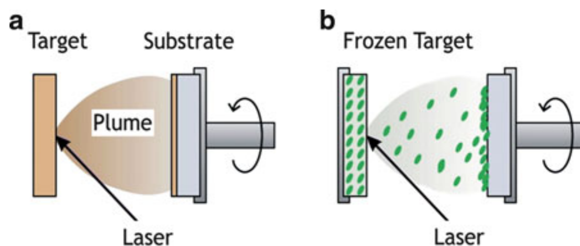


**Fig. 5.10** Polymer film deposition by (**a**) PLD and (**b**) matrix-assisted pulsed laser evaporation (MAPLE). Image courtesy of Romain Fardel

do not allow the deposition of patterns, except when using a mask. To overcome this problem, the laser-induced forward transfer for organic material has been developed [91, 92]. Here, the laser forward transfer is realized by positioning a receiver substrate in front of the donor film to recover the ejected material by irradiating from the back.

### 5.5.3 Film Pattern Transfer

The defined shape of an excimer laser beam enables to transfer precise patterns, i.e., transfer of a layer from a donor to a receiver substrate while conserving the shape defined by the laser spot. This technique is called laser-induced forward transfer (LIFT) and is illustrated in Fig. 5.11a. The donor substrate is prepared by coating a film onto a transparent plate. The receiver substrate, where the material will be deposited, is placed in front of the donor film. To obtain a shape conserving transfer of the donor material, it is illuminated from the back of the substrate with the laser beam. The material is ejected as a flyer and redeposited onto the receiver substrate. Ideally, the ablation conditions for the donor film are such that the film is ejected in a compact flyer and collected in one piece on the receiver substrate. This is shown in the shadowgraphy images in Fig. 5.12 where a stable and planar polymer flyer is observed up to 0.8 μs, at a later time, the flyer starts to disintegrate [93]. The distance between the donor and receiver substrate must also be optimized to prevent a lateral spread of the ablated material. In this way, the shape of the deposited pattern corresponds to the ablated spot, and the technique allows the transfer of a structure without using a masking technique. This technique is known as a direct writing technology [94]. The main disadvantage of this method is the direct ablation of the transfer material at the interface of the transfer. This may have a detrimental effect, i.e., decomposition, on the transfer material, especially if sensitive materials are used.

To reduce or even completely avoid the thermal decomposition of the ablated polymer, a sacrificial layer can be added to the polymer layer which absorbs all the laser energy, decomposes, and the pressure build-up transfers the polymer across a gap onto the receiver substrate. Likewise, a pattern transfer can be achieved with the receiver substrate in contact with the film. This sacrificial layer is also called a DRL and the working principle is illustrated in Fig. 5.11b. The DRL can be a metal, ceramic, or a polymer depending on the application. A polymer has the advantage

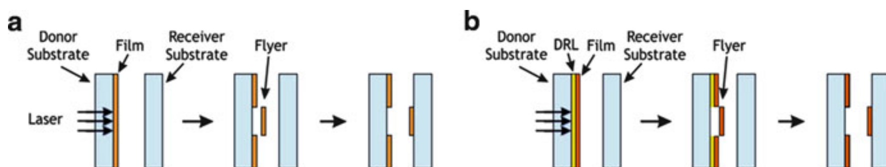


**Fig. 5.11** Working principle of (**a**) the laser-induced forward transfer and (**b**) the dynamic release layer laser-induced forward transfer (DRL-LIFT). Images courtesy of Romain Fardel

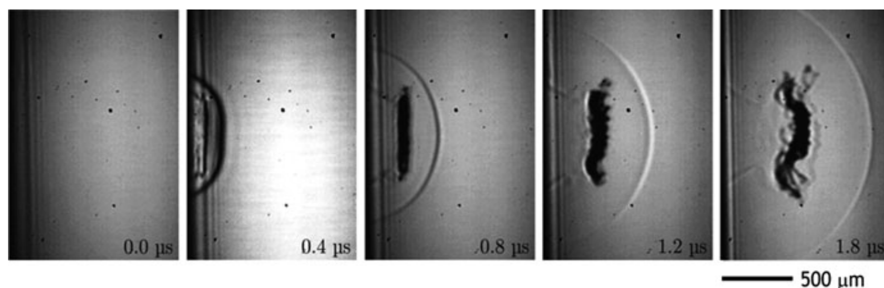


**Fig. 5.12** Sequence of pictures taken for back side ablation of a 460 nm triazene polymer film at a laser fluence of 110 mJ/cm$^2$. The time delays are indicated on the frames [93]

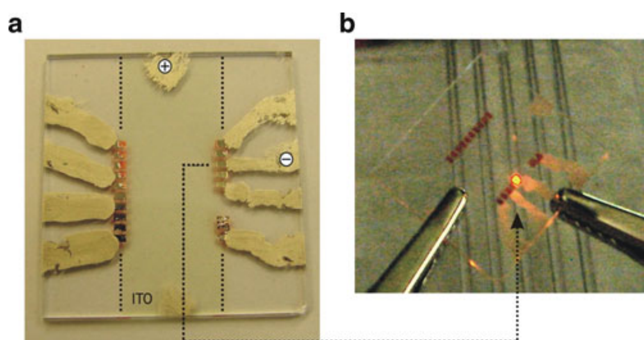


**Fig. 5.13** Overview of an organic light emitting diode (OLED) pixel realized by laser transfer. (**a**) top view of the lay-out, (**b**) pixel in operation under inert atmosphere. Noncontacted pixels also visible. Images courtesy of Romain Fardel

that upon complete decomposition into gaseous products, no contaminants can be incorporated into the transferred film while the application of UV-light reduces the thermal load to the transferred film.

Combining the UV sensitivity of triazene-polymers with the laser-induced forward transfer, the preparation of organic light emitting diode (OLED) based on polymers has been successfully demonstrated. These polymer OLEDs are fully functional without thermal or UV degradation [95] (Fig. 5.13). In Fig. 5.13a, a top view of the layout is shown indicating the pixel which is operated in Fig. 5.13b. The glass substrate is coated with a strip of indium-tin-oxide (ITO) as a transparent, conducting bottom electrode. The same approach using DRL-LIFT has been utilized to transfer biological material [96], nano-quantum dots [97], metals [98], and ceramics [99].

## 5.6 Conclusions

In this chapter, the evaporation of matter based on pulsed lasers has been introduced and advantages as well as disadvantages of this technique discussed. Next, the initial ablation processes and plume formation were introduced and the plume formation and expansion in vacuum and with a background pressure were presented in detail. Often, PLD is a tool to grow thin epitaxial films. Therefore, models and examples of thin film growth have been presented. The growth of $LaAlO_3/SrTiO_3$ heterostructures has been discussed separately to show one example for interface engineered thin film structures with remarkable properties where many aspects of thin film growth can be studied and discussed. Finally, the last section discusses the ablation of polymers which holds quite some promise for, e.g., the controlled deposition of polymer OLED pixels.

**Acknowledgements** The authors would like to thank S. Heiroth, I. Marozau, R. Fardel, M. Nagel, F. Nüesch, P.R. Willmott, S.A. Pauli, S. Thiel, G. Hammerl, J. Mannhart, L. Fitting Kourkoutis, and D.A. Muller for valuable discussions and interactions and also providing us with figures. Financial support of the Paul Scherrer Institut and the Swiss National Science Foundation are greatly acknowledged.

## References

1. D. Chrisey, G.K. Hubler, *Pulsed Laser Deposition of THIN Films*, vol. 154–155 (Wiley, New York, 1994)
2. P.R. Willmott, J.R. Huber, Rev. Mod. Phys. **72**, 315 (2000)
3. X. Yang, Y. Tang, M. Yu, Q. Qin, Thin Solid Films **358**, 187 (2000)
4. M. Braic, M. Balaceanu, A. Vladescu, A. Kiss, V. Braic, G. Epurescu, G. Dinescu, A. Moldovan, R. Birjega, M. Dinescu, Appl. Surf. Sci. **253**, 8210 (2007)
5. P.R. Willmott, R. Timm, J.R. Huber, J. Appl. Phys. **82**, 2082 (1997)
6. X.Y. Wang, D.M. Rice, Y.S. Lee, M.C. Downer, Phys. Rev. B **50**, 8016 (1994)
7. M.J. Montenegro, K. Conder, M. Döbeli, T. Lippert, P.R. Willmott, A. Wokaun, Appl. Surf. Sci. **252**, 4642 (2006)
8. I. Marozau, A. Shkabko, G. Dinescu, M. Döbeli, T. Lippert, D. Logvinovich, M. Malle-pell, C.W. Schneider, A. Weidenkaff, A. Wokaun, Appl. Surf. Sci. **255**, 5252 (2009)
9. I. Marozau, M. Döbeli, T. Lippert, D. Logvinovich, M. Mallepell, A. Shkabko, A. Wei-denkaff, A. Wokaun, Appl. Phys. A **89**, 933 (2007)
10. V. Vitiello, S. Amoruso, A. Sambri, X. Wang, Appl. Surf. Sci. **252**, 4712 (2006)
11. S. Amoruso, G. Ausanio, C. de Lisio, V. Iannotti, M. Vitiello, X. Wang, L. Lanotte, Appl. Surf. Sci. **247**, 71 (2005)
12. S. Amoruso, G. Ausanio, R. Bruzzese, M. Vitiello, X. Wang, Phys. Rev. B **71**, 033406 (2005)
13. J. Perrière, C. Boulmer-Leborgne, R. Benzerga, S. Tricot, J. Phys. D Appl. Phys. **40**, 7069 (2007)
14. T. Ishiguro, T. Shoji, H. Inada, Appl. Phys. A **69**, 149 (1999)
15. S.I. Anisimov, B.S. Luk'yanchuk, A. Luches, Appl. Surf. Sci. **96–98**, 24 (1996)
16. S. Amoruso, R. Bruzzese, N. Spinelli, R. Velotta, J. Phys. B At. Mol. Opt. Phys. **32**, 131 (1999)
17. S. Canulescu, E.L. Papadopoulou, D. Anglos, Th. Lippert, C.W. Schneider, A. Wokaun, J. Appl. Phys. **6**, 493 (2009)
18. S. Amoruso, V. Berardi, R. Bruzzese, N. Spinelli, X. Wang, Appl. Surf. Sci. **127–129**, 953 (1998)

19. L. Torrisi, F. Caridi, D. Margarone, A. Picciotto, A. Mangione, J.J. Beltrano, Appl. Surf. Sci. **252**, 6383 (1990)
20. S. Canulescu, Th. Lippert, A. Wokaun, Appl. Phys. A **93**, 771 (2008)
21. J.C.S. Kools, T.S. Baller, S.T. DeZwart, J. Dieleman, J. Appl. Phys. **71**, 4547 (1999)
22. M. Kawasaki, K. Takahashi, T. Maeda, R. Tsuchiya, M. Shinohara, O. Ishiyama, T. Yonezawa, M. Yoshimoto, H. Koinuma, Science **226**, 1540 (1994)
23. G. Koster, B.L. Kropman, G. Rijnders, D.H.A. Blank, H. Rogalla, Appl. Phys. Lett. **73**, 2920 (1998)
24. T. Ohnishi, K. Takahashi, M. Nakamura, M. Kawasaki, M. Yoshimoto, H. Koinuma, Appl. Phys. Lett. **74**, 2531 (1999)
25. S. Bals, G. Rijnders, D.H.A. Blank, G. Van Tendeloo, Phys. C **355**, 225 (2001)
26. A. Schmehl, F. Lichtenberg, H. Bielefeldt, J. Mannhart, Appl. Phys. Lett. **82**, 3077 (2003)
27. M. Huijben, G. Rijnders, D.H.A. Blank, S. Bals, S. Van Aert, J. Verbeeck, G. Van Tendeloo, A. Brinkman, H. Hilgenkamp, Nat. Mater. **5**, 556 (2006)
28. R.E. Teece, J.S. Horwitz, J.H. Claassen, D.B. Chrisey, Appl. Phys. Lett. **65**, 2860 (1994)
29. G. Cappuccio, U. Gambardella, A. Morone, S. Orlando, G.P. Parisi, Appl. Surf. Sci. **109–110**, 399 (1997)
30. J.L. Batsone, *Atomic Level Properties of Interface Materials*, vol. 83 (Chapman and Hall, London, 2008), p. 38003
31. J.A. Venables, G.D.T. Spiller, M. Hanbucken, Rep. Prog. Phys. **47**, 399 (1984)
32. C. Gerber, D. Anselmetti, J.G. Bednorz, J. Mannhart, D.G. Schlom, Nature **350**, 279 (1991)
33. I. Sunagawa, P. Bennema, *Preparation and Properties of Solid State Materials*, vol. 7 (Dekker, New York, 1982)
34. S. Thiel, G. Hammerl, A. Schmehl, C.W. Schneider, J. Mannhart, Science **313**, 1942 (2006)
35. C.W. Schneider, S. Thiel, G. Hammerl, C. Richter, J. Mannhart, Appl. Phys. Lett. **89**, 122101 (2006)
36. J.M. Dekkers, G. Rijnders, S. Harkema, H.J.H. Smilde, H. Hilgenkamp, H. Rogalla, D.H.A. Blank, Appl. Phys. Lett. **83**, 5199 (2003)
37. J.R. Kirtley, C.C. Tsuei, A. Ariando, C.J.M. Verwijs, S. Harkema, H. Hilgenkamp, Nat. Phys. **2**, 160 (2006)
38. A. Ohtomo, D.A. Muller, J.L. Grazul, H.Y. Hwang, Nature **419**, 378 (2002)
39. A. Ohtomo, H.Y. Hwang, Nature **427/441**, 423/120 (2004/2006)
40. Y. Hotta, T. Susaki, H.Y. Hwang, Phys. Rev. Lett. **99**, 236805 (2007)
41. N. Reyren, S. Thiel, A.D. Caviglia, L. Fitting-Kourkoutis, G. Hammerl, C. Richter, C.W. Schneider, T. Kopp, A.-S. Rüetschi, D. Jaccard, M. Gabay, D.A. Muller, J.-M. Tris-cone, J. Mannhart, Science **317**, 1196 (2007)
42. G. Herranz, M. Basletic, M. Bibes, C. Carrétéro, E. Tafra, E. Jacquet, K. Bouzehouane, C. Deranlot, A. Hamzic, J.-M. Broto, A. Barthtélémy, A. Fert, Phys. Rev. Lett. **98**, 216803 (2007)
43. A. Kalabukhov, R. Gunnarsson, J. Börjesson, E. Olsson, T. Claeson, D. Winkler, Phys. Rev. B **75**, 121404 (2007)
44. W. Siemons, G. Koster, H. Yamamoto, W.A. Harrison, G. Lucovsky, T.H. Geballe, D.H.A. Blank, M.R. Beasley, Phys. Rev. Lett. **98**, 196802 (2007)
45. S. Okamoto, A.J. Millis, Nature **428**, 630 (2004)
46. A. Brinkman, M. Huijben, M. van Zalk, J. Huijben, U. Zeitler, J.C. Maan, W.G. van der Wiel, G. Rijnders, D.H.A. Blank, H. Hilgenkamp, Nat. Mater. **6**, 493 (2007)
47. A.D. Caviglia, S. Gariglio, N. Reyren, D. Jaccard, T. Schneider, M. Gabay, S. Thiel, G. Hammerl, J. Mannhart, J.-M. Triscone, Nature **456**, 624 (2008)
48. J. Mannhart, D.H.A. Blank, H.Y. Hwang, A.J. Millis, J.-M. Triscone, MRS Bull. **30**, 1027 (2008)
49. S. Thiel, C.W. Schneider, F.L. Kourkoutis, D.A. Muller, N. Reyren, A.D. Caviglia, S. Gariglio, J.-M. Triscone, J. Mannhart, Phys. Rev. Lett. **102**, 046809 (2009)
50. S. Thiel, Study of interface properties in $LaAlO_3/SrTiO_3$ heterostructures. Ph.D. thesis, University of Augsburg (2009)

51. P.R. Willmott, S.A. Pauli, R. Herger, C.M. Schlepütz, D. Martoccia, B.D. Patterson, B. Delley, R. Clarke, D. Kumah, C. Cionca, Y. Yacoby, Phys. Rev. Lett. **99**, 155502 (2007)
52. C. Cen, S. Thiel, J. Mannhart, J. Levy, Science **323**, 1026 (2009)
53. C. Cen, S. Thiel, G. Hammerl, C.W. Schneider, K.E. Andersen, C.S. Hellberg, J. Mannhart, J. Levy, Nat. Mater. **7**, 298 (2008)
54. R. Srinivasan, V. Mayne-Banton, Appl. Phys. Lett. **41**, 576 (1982)
55. Y. Kawamura, K. Toyoda, S. Namba, Appl. Phys. Lett. **40**, 374 (1982)
56. A. Schawlow, Science **149**, 13 (1965)
57. G.A. Moo-Young, West J. Med. **143**, 745 (1985)
58. T. Lippert, A. Wokaun, J. Stebani, O. Nuyken, J. Ihlemann, Angew. Makromol. Chem. **206**, 97 (1993)
59. T. Lippert, Adv. Polym. Sci. **168**, 51 (2004)
60. T. Lippert, J. Dickinson, Chem. Rev. **103**, 453 (2003)
61. K. Suzuki, M. Matsuda, T. Ogino, N. Hayashi, T. Terabayashi, K. Amemiya, Excimer Lasers Opt. Appl. **2992**, 98 (1997)
62. N. Hayashi, K. Suzuki, M. Matsuda, T. Ogino, Y. Tomita, Excimer Lasers Opt. Appl. **2992**, 129 (1997)
63. S. Anisimov, B. Luk'yanchuk, Physics-Uspekhi **45**, 293 (2002)
64. N.M. Bityurin, B. Luk'yanchuk, M. Hong, T. Chong, Chem. Rev. **103**, 519 (2003)
65. M. Prasad, P.F. Conforti, B.J. Garisson, J. Appl. Phys. **101**, 103113 (2007)
66. N. Mansour, K. Jamshidi-Ghaleh, J. Phys. D Appl. Phys. **38**, 852 (2005)
67. M. Castex, N.M. Bityurin, Appl. Surf. Sci. **197–198**, 805 (2002)
68. H. Schmidt, J. Ihlemann, B. Wolff-Rottke, K. Luther, J. Troe, J. Appl. Phys. **83**, 5458 (1998)
69. G. Pettit, R. Sauerbrey, Appl. Phys. A **56**, 51 (1993)
70. M. Hauer, D.J. Funk, T. Lippert, A. Wokaun, Appl. Surf. Sci. **208**, 107 (2003)
71. G. Bounos, A. Selimis, S. Georgiou, E. Rebollar, M. Castillejo, N.M. Bityurin, J. Appl. Phys. **100**, 114323 (2006)
72. N.M. Bityurin, in *Proc. SPIE*, vol. 4423 (Chapman and Hall, London, 2001), p. 197
73. N. Arnold, N.M. Bityurin, D. Bäuerle, Appl. Surf. Sci. **138–139**, 212 (1999)
74. N.M. Bityurin, N. Arnold, B. Luk'yanchuk, D. Bäuerle, Appl. Surf. Sci. **127–129**, 164 (1998)
75. B. Luk'yanchuk, N.M. Bityurin, S. Anisimov, A.Y. Malyshev, N. Arnold, D. Bäuerle, Appl. Surf. Sci. **106**, 120 (1996)
76. N. Arnold, N. Bityurin, Appl. Phys. A **68**, 615 (1999)
77. C. Latkoczy, D. Günther, J. Anal. At. Spectrom. **17**, 1264 (2002)
78. J. Koch, M. Wälle, J. Pisonero, D. Günther, J. Anal. At. Spectrom. **21**, 932 (2006)
79. M. Tanner, D. Günther, J. Anal. At. Spectrom. **21**, 941 (2006)
80. N. Matsumoto, H. Shima, T. Fujii, F. Kannari, Appl. Phys. Lett. **71**, 2469 (1997)
81. G. Blanchet, Macromolecules **28**, 4603 (1995)
82. D. Chrisey, A. Piqué, R. McGill, J. Horwitz, B. Ringeisen, D. Bubb, P. Wu, Chem. Rev. **103**, 553 (2003)
83. E. Süske, T. Scharf, T. Junkers, M. Buback, H.U. Krebs, J. App. Phys. **100**, 014906 (2006)
84. B. Lösekrug, A. Meschede, H.U. Krebs, Appl. Surf. Sci. **254**, 1312 (2007)
85. D. Chrisey, A. Piqué, J. Fitz-Gerald, R. Auyeung, R. McGill, H. Wu, M. Duignan, Appl. Surf. Sci. **154–155**, 593 (2000)
86. A. Purice, J. Schou, P. Kingshott, N. Pryds, M. Dinescu, Appl. Surf. Sci. **253**, 7952 (2007)
87. A. Purice, J. Schou, P. Kingshott, N. Pryds, M. Dinescu, Appl. Surf. Sci. **253**, 6451 (2007)
88. S. Johnson, C. Bowie, B. Ivanov, H. Park, R. Haglund Jr., Proc. SPIE **6486**, 64860 (2007)
89. B. Toftmann, M.R. Papantonakis, R.C.Y. Auyeung, W. Kim, S.M. O'Malley, D.M. Bubb, J.S. Horwitz, J. Schou, P.M. Johansen, R.F. Haglund, Thin Solid Films **453–454**, 177 (2004)
90. S.L. Johnson, H.K. Park, R.F. Haglund Jr., Appl. Surf. Sci. **253**, 6430 (2007)
91. J. Bohandy, B.F. Kim, F.J. Adrian, J. Appl. Phys. **60**, 1538 (1986)
92. K. Kyrkis, A. Andreadaki, D. Papazoglou, I. Zergioti , *Recent advances in Laser Processing of Materials*, vol. 241 (Elsevier, Amsterdam, 2006)
93. R. Fardel, M. Nagel, F. Nüesch, T. Lippert, A. Wokaun, Appl. Surf. Sci. **255**, 5430 (2009)
94. C. Arnold, P. Serra, A. Piqué, MRS Bull. **32**, 23 (2007)

95. R. Fardel, M. Nagel, F. Nüesch, T. Lippert, A. Wokaun, Appl. Phys. Lett. **91**, 061103 (2007)
96. A. Doraiswamy, R. Narayan, T. Lippert, L. Urech, A. Wokaun, M. Nagel, B. Hopp, M. Dinescu, R. Modi, R. Auyeung, D. Chrisey, Appl. Surf. Sci. **252**, 4743 (2006)
97. J. Xu, J. Liu, D. Cui, M. Gerhold, A.Y. Wang, M. Nagel, T.K. Lippert, Nanotech. **18**, 025403 (2007)
98. R. Fardel, M. Nagel, T. Lippert, F. Nüesch, A. Wokaun, Appl. Surf. Sci. **254**, 1322 (2007)
99. D.P. Banks, K. Kaur, R. Gazia, R. Fardel, M. Nagel, T. Lippert, R.W. Eason, Europhys. Lett. **83**, 38003 (2008)